Global asteroseismology of 20,000 red giants in the TESS Continuous Viewing Zones

K. R. Sreenivas,[1]★ Timothy R. Bedding,[1] Daniel Huber[1,2], Dennis Stello[3], Marc Hon[4], Claudia Reyes[5], Yaguang Li[2], Daniel Hey[2]

[1] *Sydney Institute for Astronomy, School of Physics, University of Sydney, NSW 2006, Australia.*
[2] *Institute for Astronomy, University of Hawai'i, 2680 Wood-lawn Drive, Honolulu, HI 96822, USA*
[3] *School of Physics, University of New South Wales, Sydney, NSW 2052, Australia.*
[4] *Kavli Institute for Astrophysics and Space Research, Massachusetts Institute of Technology, 77 Massachusetts Avenue, Cambridge, MA 02139, USA*
[5] *Research School of Astronomy and Astrophysics, Australian National University, Canberra, Australian Capital Territory, Australia*

Accepted XXX. Received YYY; in original form ZZZ

ABSTRACT

With continuous observations around both ecliptic poles, TESS (Transiting Exoplanet Survey Satellite) has produced long-term photometry for millions of stars. In this work, we present an asteroseismic catalogue of 20,142 red giants in the TESS Continuous Viewing Zones. We visually assessed the power spectra for oscillations, and then applied the computationally efficient `nuSYD` method to confirm reliability. We identified an increase of 80% in the number of previously known oscillating red giants at a TESS magnitude > 8. We determined the frequency of maximum power ($\nu_{\rm max}$) and the large frequency separation ($\Delta\nu$) using pySYD, achieving typical precisions of 1.3 % and 0.9 %, respectively. We classified the stars into Red Giant Branch (RGB) and Core Helium Burning (CHeB) classes using a Convolutional Neural Network. Together with spectroscopic data for 10987 stars with reliable asteroseismic measurements, we estimated the mass, radius, and surface gravity of the stars, with typical precisions comparable to that of *Kepler*. A comparison of the seismic radii with Gaia radii shows excellent agreement. We have been able to improve the precision on stellar mass and radii relative to previous studies. With three years of TESS data, the asteroseismic parameters are precise enough to identify the RGB bump and delineate the Zero Age Helium Burning edge. Combined with astrometric data, these parameters reveal established trends across the Galactic plane, providing a valuable set of uniformly determined asteroseismic parameters for Galactic Archaeology.

Key words: keyword1 – keyword2 – keyword3

1 INTRODUCTION

Asteroseismology, the study of stars through sound waves propagating within their interiors, has significantly advanced our understanding of stellar structure and evolution. These standing waves, which result from the stochastic excitation and damping caused by stellar convection, provide valuable information about both the interiors and surface properties of stars. Observationally, these waves appear as distinct frequencies in Fourier space, forming a Gaussian-shaped power excess. This feature is characterized by two key parameters: the frequency of maximum power ($\nu_{\rm max}$) and the large frequency separation ($\Delta\nu$) (Ulrich 1986; Brown et al. 1991; Kjeldsen & Bedding 1995). The frequency $\nu_{\rm max}$ is approximately proportional to the acoustic cutoff frequency, which is itself a function of the star's surface gravity and effective temperature. The large frequency separation, $\Delta\nu$, reflects the average density of the star. The scaling relations connect these two frequencies to fundamental stellar parameters, allowing the determination of a star's mass, radius, and surface gravity (Stello et al. 2008; Kallinger et al. 2010a). These scaling relations have been extensively validated using radial velocity and photometric data, and they have proven to be a reliable method for determining precise stellar parameters in red giants.

The long-baseline photometry provided by space missions such as *CoRoT* and *Kepler* (Baglin et al. 2006; Borucki et al. 2010) has revolutionized our understanding of red giants over the past decade. Ensemble studies of red giants (Chaplin & Miglio 2013; Jackiewicz 2021; Noels-Grotsch & Miglio 2025) have demonstrated the power of precise photometry in characterizing stellar evolutionary states, internal structures, and rotation properties (Bedding et al. 2011; Vrard et al. 2016; Mosser et al. 2017; Gehan et al. 2018). Yu et al. (2018) produced a catalogue of 16,000 *Kepler* red giants and revealed a significant dependence of solar-like oscillation amplitudes on metallicity and mass. In conjunction with simulations, Li et al. (2021) used *Kepler* red giant data to validate asteroseismic scaling relations and quantify the intrinsic scatter in these relations. Additionally, *Kepler* observations established a metallicity-dependent trend in the scaling relation for the frequency of maximum power ($f_{\nu_{\rm max}}$) (Li et al. 2024). These datasets were used to advance our understanding of red giants at a population level. They also supported the development of methods for asteroseismic analysis of large-scale datasets Hon et al. (2018a, 2021); Sreenivas et al. (2024). Because of the precise nature of asteroseismic measurements, these datasets enabled studies of the

★ E-mail: skal9597@uni.sydney.edu.au

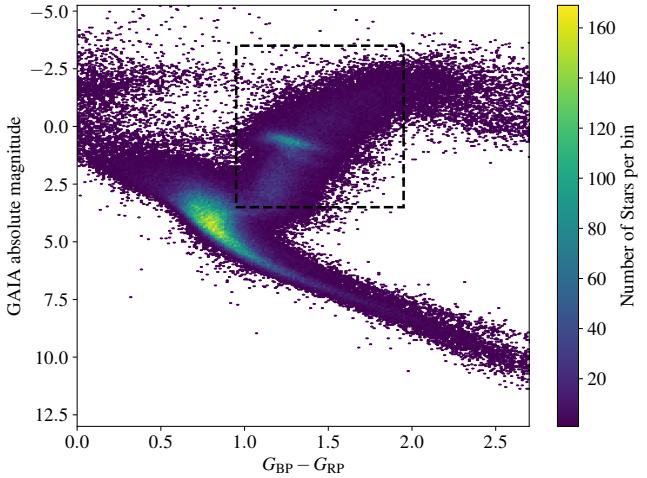

Figure 1. Colour-magnitude diagram using Gaia apparent magnitudes of all stars with TESS magnitude brighter than 13.5. The rectangle shows the 72,647 stars selected for analysis in this work.

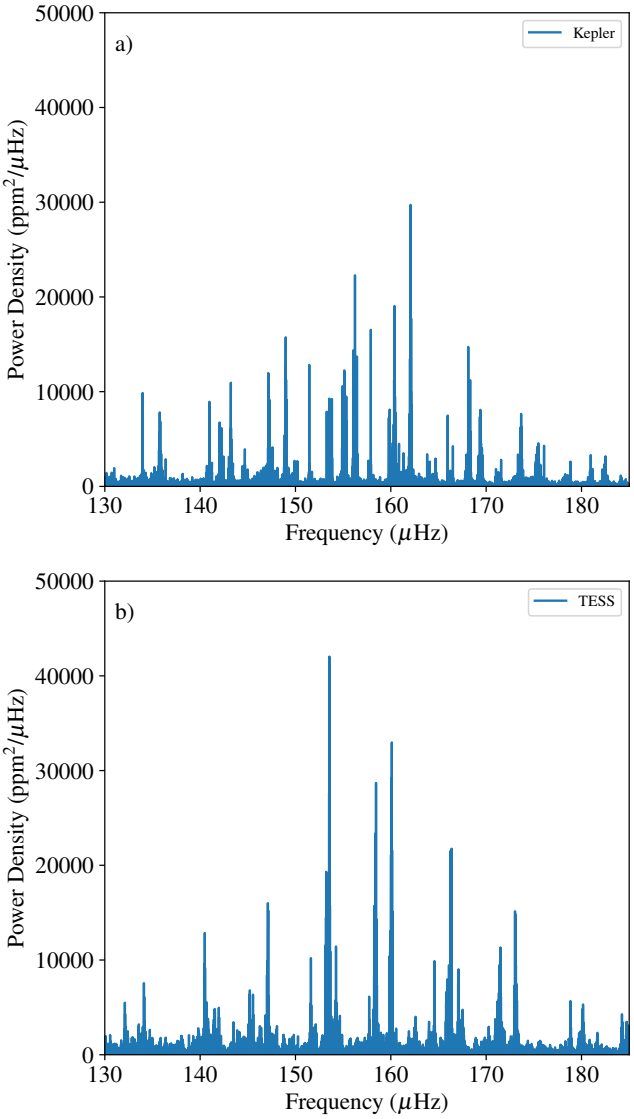

Figure 2. Solar like oscillations of a typical red giant. Panel a shows the power density spectra of an oscillating *Kepler* red giant (KIC 9075872) and Panel b for an oscillating red giant (TIC 237197414) in the northern TESS CVZ.

solar neighbourhood and the mapping of our Galaxy (Miglio et al. 2012; Anders et al. 2017; Zinn et al. 2022; Pinsonneault et al. 2025).

While previous space missions, such as *CoRoT* and *Kepler*, focused on specific regions of the sky, the Transiting Exoplanet Survey Satellite (TESS, Ricker et al. 2015) instead observes nearly the entire sky, producing light curves with typical baselines of 27 days per sector. This broad sky coverage has enabled TESS to detect oscillations in thousands of red giants across the sky (Hon et al. 2021; Mackereth et al. 2021; Hatt et al. 2023; Zhou et al. 2024; Grusnis et al. 2025). However, due to its small aperture size and short observation baselines for most fields, TESS is less effective at detecting oscillations in faint (Tmag> 10) high-ν_{max} red giants (Stello et al. 2022). At the same time, the higher-amplitude low-ν_{max} stars require longer baseline for localizing power excess. However, TESS's wide field of view and observing strategy create two Continuous Viewing Zones (CVZs), each covering 452.16 deg^2 around the ecliptic poles: the Southern CVZ (ecliptic latitude < −78 degrees, SCVZ) and the Northern CVZ (ecliptic latitude > 78 degrees, NCVZ). The SCVZ benefits from a longer observing baseline, with light curves spanning 3 years, while the NCVZ has 2 years of continuous observations due to TESS's initial focus on the southern sky.

In this work, we present a catalogue of oscillating red giants in TESS's CVZs, with asteroseismic masses and radii determined homogeneously. By focusing on this region, we aim to expand the sample of distant, low-luminosity red giants for use in future investigations.

.

2 DATA

2.1 Sample selection

From the TESS Input catalogue (TIC, version 8.2, Paegert et al. 2022), we selected all stars with ecliptic latitude < −78 (SCVZ) and > 78 (NCVZ). Due to the limited availability of light curves at fainter magnitudes and the difficulty in detecting oscillations, we restricted our sample to stars with TESS magnitude (Tmag) less than 13.5. We removed the duplicate entries by setting `q_Gaia = 1` and `Disposition = NULL` columns in the TIC. The first criterion ensures that the stars have reliable astrometric information from Gaia, and the later one ensures that the entries are unique. Figure 1 shows the colour-magnitude diagram using the absolute magnitude (M_G) and the dereddened colour indices from Gaia DR2 (Gaia Collaboration et al. 2018) information from TIC. We selected all stars with $-3 < M_G < 4$ and $1 < G_{BP} - G_{RP} < 2$, which left us with 72,647 possible red giants. As can be seen from the figure, such a selection includes stars from the lower to the upper red giant branch, and the red clump, on which this study will be focused.

2.2 Light curves and power density spectra

TESS observes the sky in 27-d sectors, producing Full Frame Images (FFIs) containing a large number of stars. During the first cycle of the mission, the FFIs were produced at a cadence of 30 minutes, which was later reduced to 10 min (cycle 2) and then to 200 seconds. Two

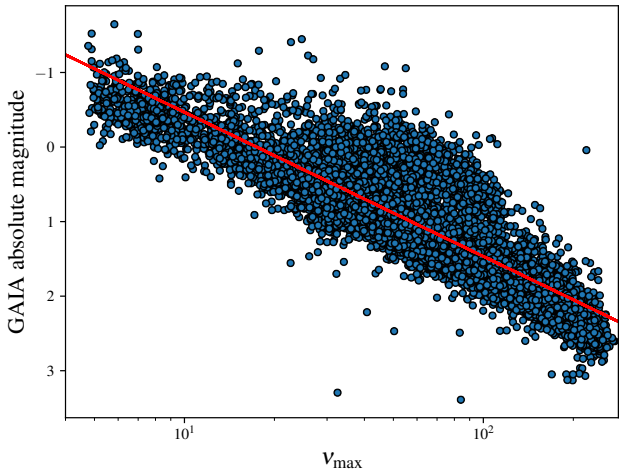

Figure 3. Gaia Absolute Magnitude vs Frequency of Maximum power for all 16000 *Kepler* stars in Yu et al. (2018). The red line corresponds to the fit provided in eqn. 1.

of the widely used light curve products from these FFIs are TESS-SPOC (Jenkins et al. 2016; Caldwell et al. 2020) and QLP (Huang et al. 2020a,b). Although QLP light curves are available across a greater number of sectors, Sreenivas et al. (2025) demonstrated that TESS-SPOC light curves typically has lower noise levels.

For each star, we used TESS-SPOC light curves whenever available for a given sector and used QLP otherwise. This ensures that we maintain higher frequency resolution, while also ensuring good quality of the data. We discarded cadences associated with any anomalies by setting the `quality` flag to 0 [1]. The light curves were high-pass filtered using a Gaussian kernel with a sigma of 5 days to remove low-frequency signals, and a 5-sigma clipping was applied to remove outliers. The power spectra were calculated using the astropy Lomb–Scargle periodogram (Press & Rybicki 1989), and converted to power density by multiplying by the effective observation time. We calculated the power spectrum up to 283.4,μHz, corresponding to the Nyquist frequency of the FFIs with a cadence of 30 min (Sreenivas et al. 2025). Figure 2 compares the power density spectra of an oscillating red giant in *Kepler* (top panel) and in the TESS CVZ (bottom panel). It can be seen that the oscillations in the TESS power spectrum has similar amplitudes, as to that from 4-yr *Kepler* data.

3 DETECTION AND ESTIMATION OF GLOBAL ASTEROSEISMIC PARAMETERS

3.1 Identifying oscillating red giants

In the frequency domain, solar-like oscillators show an excess of power whose shape is approximately Gaussian. Following Stello et al. (2017); Stello et al. (2022), we visually examined the power density spectra of our 72,647 stars in logarithmic space and classified the detection of oscillations as either "yes", "maybe" or "no" based on the characteristics of the power excess. This resulted in 20,285 candidate oscillating stars (11,857 yes and 8428 maybe).

[1] https://archive.stsci.edu/missions/tess/doc/EXP-TESS-ARC-ICD-TM-0014.pdf

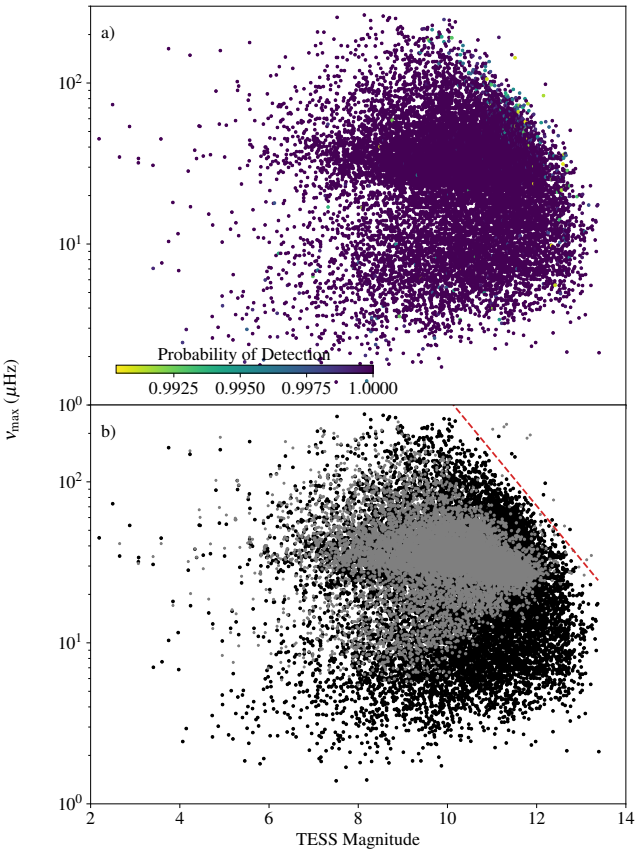

Figure 4. Frequency of Maximum power vs TESS Magnitude for all the stars in the sample. Top panel shows the stars colour coded by their detection probability. The bottom panel shows stars which were visually verified (black). The grey points are the detections from Hon et al. (2021). The dashed line shows the empirical detection limit from (Hon et al. 2021).

We next employed the `nuSYD` pipeline (Sreenivas et al. 2024), which is a simple and fast method to estimate ν_{max} for this large sample of red giants. This method requires an initial value for ν_{max}, for which we used the correlation between Gaia absolute magnitude (M_G) and ν_{max} for the 16,000 oscillating *Kepler* red giants reported by Sreenivas et al. (2024). This correlation, shown in Fig. 3, is analogous to a period-luminosity relation and allows the location of the power excess to be predicted approximately using only M_G. We fitted a line to derive this approximate relation:

$$\nu_{max}/\mu\text{Hz} = 10^{0.52M_G+1.24}. \quad (1)$$

Although this relation is very approximate (scatter $\approx$ 40 %), it is sufficient for the `nuSYD` pipeline to converge to ν_{max} if the star is oscillating. In using the pipeline, we measured the white noise at high frequencies, subtracted it from the power spectrum, and heavily smoothed the power spectra with a Gaussian kernel. We then reported the ν_{max} corresponding to the maximum of the power excess (P_{peak}) as the initial estimate of ν_{max} for the 20,285 candidate oscillators.

Having made initial estimates of ν_{max}, it is important to verify whether these are genuinely solar-like oscillators. We followed the procedure outlined by Chaplin et al. (2011) and Hey et al. (2024) to predict the empirical signal-to-noise ratio (SNR) and determine the probability of detection at the observed ν_{max}. We used the ν_{max}, the observational time span derived from our measurements, and effective temperature, G magnitude, and distance from TIC to calculate

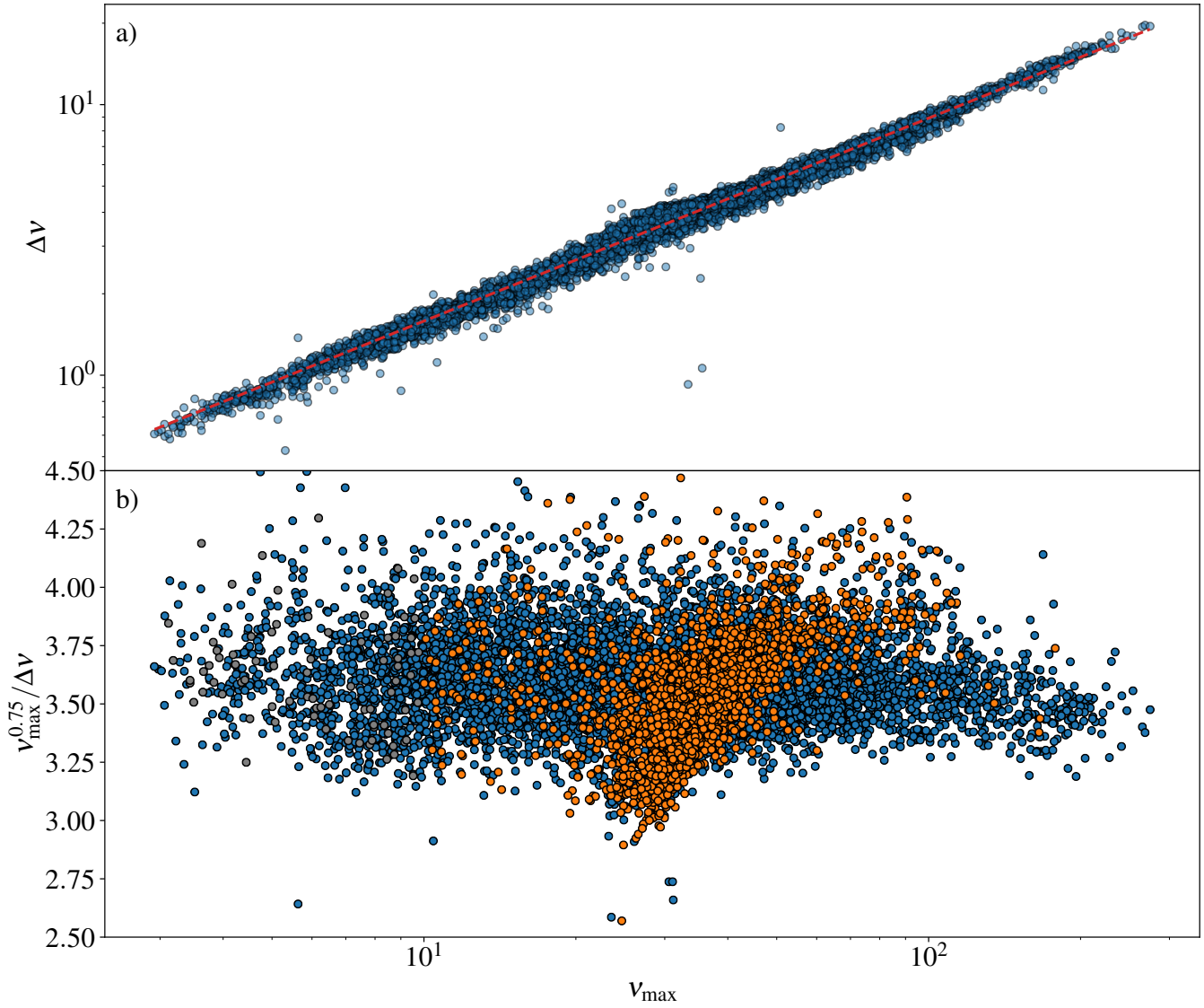

Figure 5. Panel a shows the correlation between $\nu_{\rm max}$ and $\Delta\nu$. The dashed line corresponds to a power law fit in linear space. Panel b shows the same data, where the y axis is a proxy for mass. The blue points show the 7616 Red Giant Branch (RGB) stars and orange points show the 3371 Core Helium Burning (CHeB) stars, for stars with good $\Delta\nu$ flag = 1.

the oscillation amplitude, granulation power, and instrumental noise. These computations followed the equations provided by Chaplin et al. (2011) and Campante et al. (2016). Then, the signal-to-noise ratio (SNR) was calculated as the ratio between the total oscillation power inside the oscillation envelope and the total background power. Subsequently, we determined the probability that this SNR exceeds the predicted SNR using the equations from Chaplin et al. (2011).

Oscillation amplitude scales inversely with $\nu_{\rm max}$ (Huber et al. 2011; Yu et al. 2018). To represent the relationship between signal and noise, Stello et al. (2017) introduced the $\nu_{\rm max}$ vs apparent brightness diagram. In such a diagram, the lowest SNR region appears at the top-right (with the highest SNR in the bottom-left), while the most distant stars are located in the bottom-right (with the least distant stars in the top-left). Figure 4 a shows $\nu_{\rm max}$ as a function of TESS magnitude, color-coded by detection probability, for all 20,142 stars in our sample. We find that approximately 98% of the stars have a detection probability greater than 0.99. For the remaining stars, the detection probability increased to above 0.99 when the effective temperature was chosen from Gaia `GSPPHOT`. From Figure 4 b, we observe an increase in the number of low- and high-$\nu_{\rm max}$ stars at Tmag > 8 (black circles) compared with Hon et al. (2021) (gray circles). This finding suggests that data from long-term TESS-based seismology can be used to probe even distant stars. The dashed line in Figure 4 b indicates the formal detection limit provided by Hon et al. (2021). Stars above this line, particularly those with high $\nu_{\rm max}$, have amplitudes below the noise level, which makes detecting solar-like oscillations challenging. However, we visually inspected the pixel files and confirmed that no nearby bright stars existed within a radius of 4 pixels, so we retained these stars in our sample. By comparing with panel a, we see that stars near this line have lower detection probabilities. This observation suggests that we applied conservative criteria when identifying oscillating stars during the visual inspection of their power spectra.

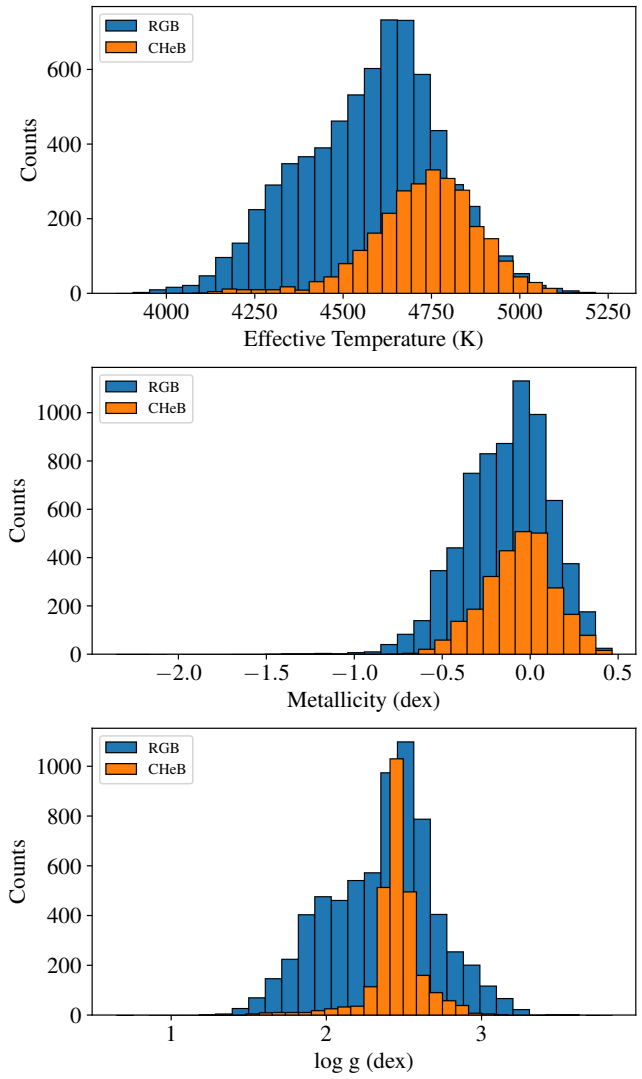

Figure 6. Distribution of stellar spectroscopic parameters from (Yu et al. 2023) for our sample, red for 7616 RGB and blue for 3371 CHeB stars. Panel a shows the effective temperature, panel b shows the metallicity and panel c shows log g.

3.2 Blend analysis

Due to the large pixel size of TESS (21.6 arcsec/pixel), a pixel could capture light from a companion star instead of the target star. If the companion star is an oscillating red giant, these oscillations would imprint their signatures on the wrong light curve. Previous studies have shown that contamination affects red giant oscillation spectra for stars fainter than a TESS magnitude of about 12 (Hon et al. 2021; Stello et al. 2022). To ensure the sample is free from false detections, we conducted a blending analysis following the procedure outlined in Stello et al. (2022). For each target star, we selected all stars within 150 arcsec and applied two criteria for identifying potential blends. We first calculated the Shape-Based Distance (SBD; Paparrizos & Gravano 2017) between the power density spectra of the target star and all other stars in the list. We identified stars with an SBD value below 1 as potential blends, indicating that their power density spectra could be similar to that of the target star. For stars in this list with $\nu_{\rm max}$ values falling within 20% of the target $\nu_{\rm max}$, we measured the mean power within an envelope of width $0.33(\nu_{\rm max}/\mu{\rm Hz})^{0.88}$ centred on $\nu_{\rm max}$. If the power difference fell within 0.5% of the entire sample, we flagged the star as contaminated. Figure 4 b shows the contaminated stars (orange points) in our sample. We identified 143 pairs of stars as contaminating, which constitutes less than 1% of the total sample. We inspected the pixel files of a few of these stars and confirmed that they fall within the same pixel. After these steps, our sample contains 20,142 oscillating red giants.

3.3 Global Asteroseismic parameters

Two of the global asteroseismic quantities that can be measured from the frequency spectra of solar-like oscillations are the frequency of maximum power ($\nu_{\rm max}$) and the large frequency separation ($\Delta\nu$). These satisfy the approximate scaling relations (Ulrich 1986; Brown et al. 1991; Kjeldsen & Bedding 1995), given by:

$$\frac{\Delta\nu}{\Delta\nu_\odot} \approx \sqrt{\frac{\rho}{\rho_\odot}} \tag{2}$$

and

$$\frac{\nu_{\rm max}}{\nu_{\rm max,\odot}} \approx \frac{g/g_\odot}{\sqrt{T_{\rm eff}/T_{\rm eff,\odot}}}. \tag{3}$$

By solving these equations, we can determine stellar mass (M), radius (R) and surface gravity (g) (Stello et al. 2008; Kallinger et al. 2010b).

$$\frac{M}{M_\odot} \approx \left(\frac{\nu_{\rm max}}{\nu_{\rm max,\odot}}\right)^3 \left(\frac{\Delta\nu}{\Delta\nu_\odot}\right)^{-4} \left(\frac{T_{\rm eff}}{T_{\rm eff,\odot}}\right)^{3/2}, \tag{4}$$

$$\frac{R}{R_\odot} \approx \left(\frac{\nu_{\rm max}}{\nu_{\rm max,\odot}}\right) \left(\frac{\Delta\nu}{\Delta\nu_\odot}\right)^{-2} \left(\frac{T_{\rm eff}}{T_{\rm eff,\odot}}\right)^{1/2} \tag{5}$$

and

$$\frac{g}{g_\odot} \approx \left(\frac{\nu_{\rm max}}{\nu_{\rm max,\odot}}\right) \left(\frac{T_{\rm eff}}{T_{\rm eff,\odot}}\right)^{1/2}. \tag{6}$$

To improve the $\nu_{\rm max}$ measurements from `nuSYD`, and to measure $\Delta\nu$ and associated uncertainties, we used the `pySYD` pipeline (Huber et al. 2009; Chontos et al. 2022). This involves modelling the stellar background at low frequency using Harvey functions and a constant term for high-frequency noise. For the purpose of measuring $\nu_{\rm max}$, we smoothed the background-corrected power density spectra with a Gaussian kernel, with a width of $\Delta\nu * \max\left(2, 4\,(\nu_{\rm max}/\nu_{\rm max,\odot})^{0.2}\right)$. We set a lower limit of $2\,\Delta\nu$ instead of the default value of $1\,\Delta\nu$ to ensure that the envelope remains smooth at low $\nu_{\rm max}$ values (Sreenivas et al. 2024). We determined $\nu_{\rm max}$ as the peak of this smoothed oscillation envelope, while $\Delta\nu$ was derived from the autocorrelation of the background-corrected spectra.

To verify the quality of the $\Delta\nu$ measurements, we used the neural network developed by Reyes et al. (2022). The network uses $\nu_{\rm max}$, $\Delta\nu$, and the background-corrected power density spectra from `pySYD` to estimate the probability that the measured $\Delta\nu$ reproduces vertical ridges in the collapsed échelle diagram. We first removed false-positive measurements that could reproduce vertical ridges, using the $\nu_{\rm max}$–$\Delta\nu$ relation (Stello et al. 2009). Stars with a probability above 0.5 were considered reliable and flagged as good $\Delta\nu$ in Table 1. This resulted in a sample of 10987 stars, or 60% of the sample, with properly measured $\Delta\nu$. Figure 5 a shows the $\nu_{\rm max}$–$\Delta\nu$ diagram for all the 10987 stars. We fitted a power law of the form $\alpha\Delta\nu^\beta$. The fitted parameters were obtained as $\alpha = 0.282 \pm 0.004$ and $\beta = 0.750 \pm 0.003$. As expected, they follow the well-known relation between $\nu_{\rm max}$ and $\Delta\nu$ first shown by Hekker et al. (2009) and Stello et al. (2009).

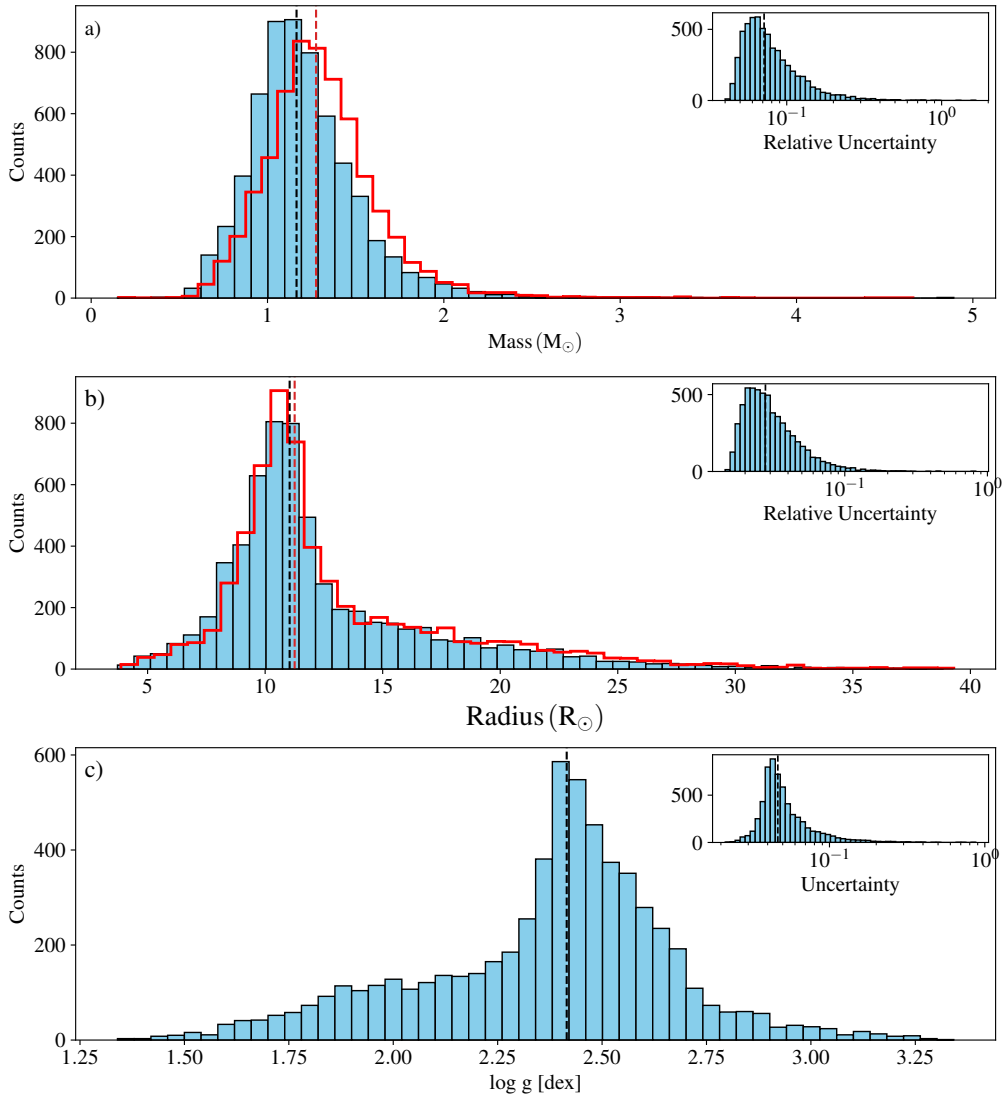

Figure 7. Distribution of Mass (top panel), Radius (middle panel) and log g (bottom panel) for the sample of stars. The insets show the uncertainty in stellar parameters. The red histograms show the distribution of uncorrected mass and radii. The dashed vertical lines show the median values of the distributions.

3.4 Determination of evolutionary states

Based on their core properties, red giants can be classified into red giant branch (RGB), which burn hydrogen in a shell surrounding the core, and core-helium-burning stars (CHeB) (see reviews by Hekker & Christensen-Dalsgaard 2017; Noels-Grotsch & Miglio 2025). Oscillation frequencies reflect the properties of the core and envelope, and the period spacing of dipole ($l = 1$) modes can be used to distinguish between RGB and CHeB stars (Bedding et al. 2011; Mosser et al. 2015). We used the Convolutional Neural Network (CNN) proposed by Hon et al. (2018a,b) to classify red giants based on the characteristics of RGB and CHeB stars in folded power spectra. The CNN uses images of the folded background-corrected power spectra and $\Delta\nu$ values to predict a score, using a network trained on labels from *Kepler* red giant data (Elsworth et al. 2019). For each input, it predicts a score between 0 and 1 for the star to be a CHeB star. In addition to this score, the network also outputs the aleatoric uncertainty, related to the error in prediction due to noise in the data (Gal & Ghahramani 2016). We classified stars with a score below 0.5 as RGB and those with a score above 0.5 as CHeB. Figure 5 b shows the results from the neural network classifier for stars with the good $\Delta\nu$ flag = 1 (see Sec. 3.3). Among this, 7616 stars were classified as RGB and 3371 stars as CHeB based on this score. We note that a small fraction of stars are classified as CHeB at lower $\nu_{\rm max}$ values. Given that low-$\nu_{\rm max}$ stars require longer observations and that core-helium burning is not expected those $\nu_{\rm max}$ values, we classify them as "ambiguous" (Stello et al. 2013; Hon et al. 2018a).

3.5 Stellar spectroscopic parameters

Accurate determination of stellar mass, radius, and surface gravity requires reliable spectroscopic estimates of effective temperature and metallicity. Several spectroscopic surveys provide parameters for most stars in our sample. The Apache Point Observatory Galactic Evolution Experiment (APOGEE) produces stellar parameters, including surface abundances, for thousands of red giants mainly in the northern hemisphere, to study chemical composition and abundances (Abdurro'uf et al. 2022). Galactic Archaeology with Hermes (GALAH) targets nearby stars in the southern hemisphere to study the

Table 1. Column describing Table of asteroseismic parameters for 20,142 oscillating red giants in cvz

Label	Description
TIC ID	TESS Input Catalog ID
GAIA ID	Source ID from GAIA DR3
ELON	Ecliptic Longitude (deg)
ELAT	Ecliptic Latitude (deg)
Tmag	TESS magnitude
Time span	Effective time span of TESS light curve (days)
Visual_class	Visual classification (1 for yes, 2 for maybe and 0 for no)
$\nu_{\rm max}$	Frequency of Maximum Power (μHz)
$e_{\nu_{\rm max}}$	Uncertainty in Frequency of maximum power (μHz)
$\Delta\nu$	Large Frequency Separation (μHz)
$e_{\Delta\nu}$	Uncertainty in Large Frequency Separation (μHz)
good $\Delta\nu$ flag	Flag indicating the reliable $\Delta\nu$ (1 for reliable and 0 for unreliable)
$P_{\Delta\nu}$	$\Delta\nu$ Vetting probability
Ev state	Evolutionary state (1 for RGB , 2 for CHeB and 0 for ambiguous)
Ev state score	Evolutionary state prediction score
$T_{\rm eff}$	Effective Temperature (K)
$e_{T_{\rm eff}}$	Uncertainty in Effective Temperature (K)
[M/H]	Metallicity (dex)
$e_{\rm [M/H]}$	Uncertainty in Metallicity (dex)
$\log g$ (spec)	Spectroscopic Surface gravity (dex)
$e_{\log g}$ (spec)	Uncertainty in Spectroscopic Surface Gravity (dex)
spec source	Source of Spectroscopic data (1 for APOGEE/GALAH/RAVE and 2 for XP Spectra)
$f_{\Delta\nu}$	Correction factor for $\Delta\nu$ scaling relation
Mass	Stellar mass ($M_\odot$)
$e_{\rm Mass}$	Uncertainty in stellar mass ($M_\odot$)
Radius	Stellar Radius ($R_\odot$)
$e_{\rm Radius}$	Uncertainty in stellar radius ($R_\odot$)
$\log g$ (seismic)	Surface Gravity (dex)
$e_{\log g}$ (seismic)	Uncertainty on surface gravity (dex)
Gold sample	Whether member of gold sample (G for member and 0 for non member)

architecture and chemistry of the Galactic neighborhood (De Silva et al. 2015). The RAdial VElocity experiment (RAVE), whose primary aim was to collect radial velocities for southern dwarfs and early giants, also provided stellar parameters for abundance studies (Steinmetz et al. 2020). Because surveys derive atmospheric parameters (effective temperature, metallicity, and surface gravity) using different methods, using parameters from different surveys can introduce systematic effects on different parameters and therefore it is essential to bring them to a uniform scale of measurement using proper calibration.

Here, we use stellar parameters from Yu et al. (2023) to calculate stellar mass, radius, and surface gravity. This catalogue provides effective temperatures and metallicities derived from APOGEE, RAVE, and GALAH spectra, which were homogeneously calibrated using common stars across the three catalogues and Gaia DR3 parallax data. For the remaining 4434 stars with good $\Delta\nu$, we used the stellar parameters from Andrae et al. (2023). These are the stellar parameters derived from the Gaia XP spectra (Carrasco et al. 2021) using the XGBoost algorithm (Chen & Guestrin 2016) which was trained using APOGEE spectroscopic parameters. This ensures that stars with reliable $\Delta\nu$ have stellar parameters in our catalogue. We compared the spectroscopic parameters with the corresponding parameters from Yu et al. (2023), and found that the median offset between them was less than 1%. As these spectroscopic parameters do not have uncertainties, we adopt an uncertainty of 2% on effective temperature, 10% on metallicity and 2% on $\log g$. Figure 6 presents the stellar parameters of 10987 stars in our sample. The distributions align with the general parameter ranges observed for red giants (Pinsonneault et al. 2018, 2025).

3.6 Determination of $f_{\Delta\nu}$

Previous studies have identified a systematic offset between stellar parameters derived using scaling relations and those determined by full asteroseismic modelling (White et al. 2011; Mosser et al. 2013; Guggenberger et al. 2016; Sharma et al. 2016; Li et al. 2023). To address this offset, two correction parameters, $f_{\Delta\nu}$ and $f_{\nu_{\rm max}}$, were included in the scaling relations (Sharma et al. 2016). The corrected scaling relations are expressed as follows:

$$\frac{M}{M_\odot} = \left(\frac{\nu_{\rm max}}{f_{\nu_{\rm max}}\nu_{\rm max,\odot}}\right)^3 \left(\frac{\Delta\nu}{f_{\Delta\nu}\Delta\nu_\odot}\right)^{-4} \left(\frac{T_{\rm eff}}{T_{\rm eff,\odot}}\right)^{3/2}. \quad (7)$$

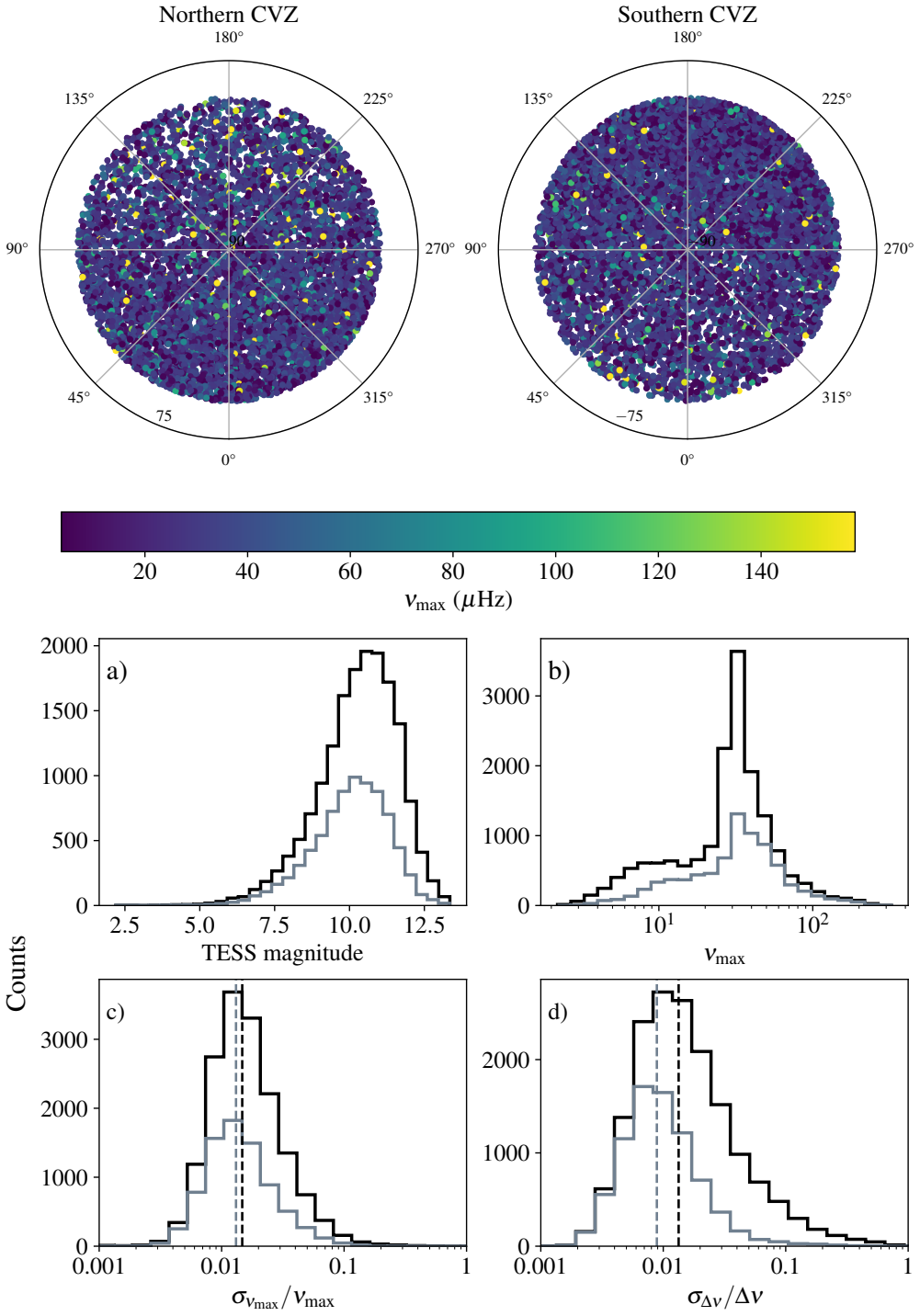

Figure 8. Properties of the stars in our final sample. The top two diagrams show the distribution of 20,142 oscillating red giants in northern CVZ and southern CVZ. Panel a shows the distribution of TESS magnitude, panel b shows the distribution of $\nu_{\rm max}$, panel c shows the fractional uncertainty on $\nu_{\rm max}$ and panel d shows the fractional uncertainty on $\Delta\nu$. The histograms in black corresponds to the full sample of red giants and grey corresponds to gold sample.

$$\frac{R}{\mathrm{R}_\odot} = \left(\frac{\nu_{\rm max}}{f_{\nu_{\rm max}}\nu_{\rm max,\odot}}\right)\left(\frac{\Delta\nu}{f_{\Delta\nu}\Delta\nu_\odot}\right)^{-2}\left(\frac{T_{\rm eff}}{T_{\rm eff,\odot}}\right)^{1/2}. \quad (8)$$

$$\frac{g}{\mathrm{g}_\odot} = \left(\frac{\nu_{\rm max}}{f_{\nu_{\rm max}}\nu_{\rm max,\odot}}\right)\left(\frac{T_{\rm eff}}{T_{\rm eff,\odot}}\right)^{1/2}. \quad (9)$$

The parameter $f_{\Delta\nu}$ accounts for the inexactness of eq. 2, which can be calculated from theoretical stellar models. For RGB and CHeB stars, we calculated the corrections using `asfgrid` (Sharma et al. 2016; Stello & Sharma 2022). This procedure used the uncorrected mass, effective temperature, metallicity, and evolutionary states as inputs, interpolated the nearest stellar model grids, and derived $f_{\Delta\nu}$. Along with the effective temperatures and metallicities from spec-

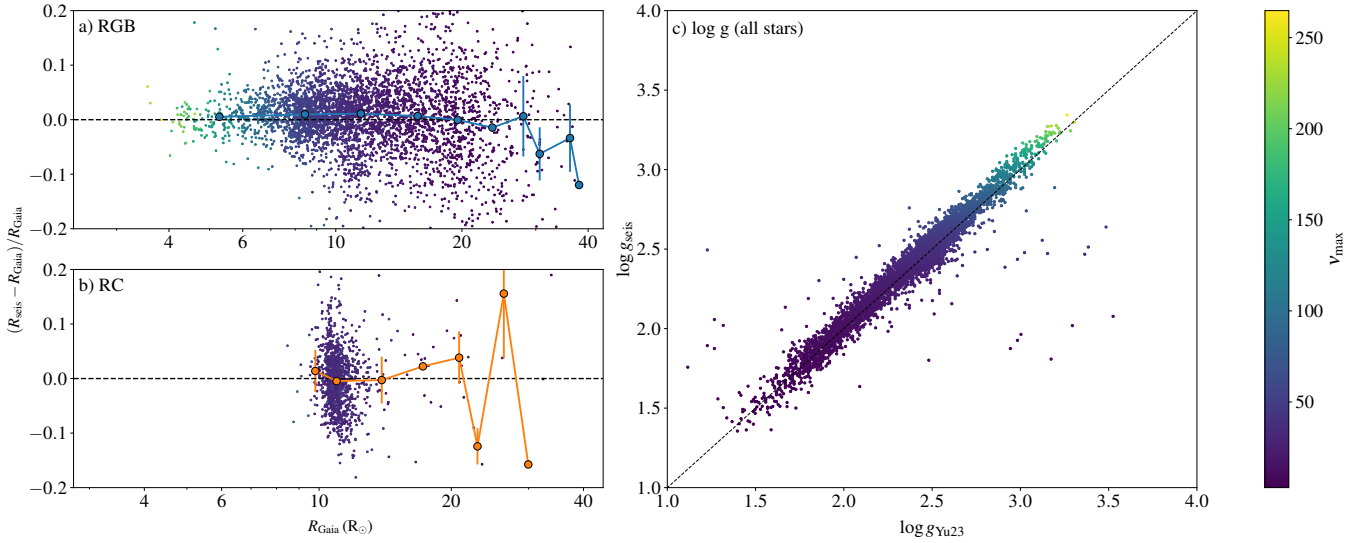

Figure 9. Comparison of asteroseismic radii with spectroscopic parameters, for the stars in gold sample. The top panel shows the comparison of GAIA radii for RGB stars and bottom panel shows the comparison for CHeB stars, both colour-coded by ν_{max}. The blue and orange lines show the median offset between asteroseismic radii determined using `asfgrid` (Sharma et al. 2016) corrections with Gaia radii for RGB and CHeB stars, respectively. The errorbars show the median absolute deviation (MAD) per bin.

troscopy, we estimated the $f_{\Delta\nu}$ parameter for 10987 stars that have reliable $\Delta\nu$ measurements. We verified that these values show clear trends with effective temperature and metallicity, as shown by Sharma et al. (2016). Following Pinsonneault et al. (2025), we assumed an uncertainty of 0.005 for the $f_{\Delta\nu}$ values [2].

Note that this approach does not include the standard surface term corrections to model frequencies, which also affects $\Delta\nu$ from models (Kjeldsen et al. 2008; Ball & Gizon 2014; Li et al. 2023). Li et al. (2023) parametrized the surface effect-corrected $f_{\Delta\nu}$ as a function of $T_{\rm eff}$ and [M/H] for RGB stars and has shown that asteroseismic radii derived using these corrections agree well with Gaia radii. However, for CHeB stars Schimak et al. (submitted) demonstrated that including surface corrections to $f_{\Delta\nu}$ does not improve the asteroseismic masses and requires further studies to quantify it. To maintain uniform parameter values for the analysis, we chose not to calculate the masses and radii using these surface corrections.

The value of $f_{\nu_{\rm max}}$ indicates the inexactness of eq. 3. Because $f_{\nu_{\rm max}}$ lacks a robust theoretical prediction from stellar models, its value is determined empirically from observations and theoretical models. Recent studies (Li et al. 2024; Larsen et al. 2025; Lundkvist et al. 2025) identified a metallicity dependence in this correction factor. Currently, corrections are derived empirically by comparing asteroseismic radii with Gaia radii. Pinsonneault et al. (2025) fitted a polynomial to the ratio of $f_{\Delta\nu}$-corrected asteroseismic radii to Gaia radii and used this relation to account for discrepancies between asteroseismic and Gaia-derived radii. Marasco et al. (2025) adopted a single value of $f_{\nu_{\rm max}}$ for all stars, defined as the median ratio between asteroseismic and Gaia radii. While early studies assumed a fixed value of unity for this correction term, more recent works calibrated it using Gaia measurements. As a reliable framework for $f_{\nu_{\rm max}}$ is not yet established, we assume $f_{\nu_{\rm max}} = 1$ to compute stellar masses and radii.

[2] Note that some authors (Pinsonneault et al. 2025; Liagre et al. 2025) adopt a definition for $f_{\Delta\nu}$ that is the inverse of that used here and by `asfgrid`.

3.7 Calculation of stellar parameters

By combining our measurements of $\nu_{\rm max}$ and $\Delta\nu$ with the effective temperatures, and including the correction $f_{\Delta\nu}$, we calculated the stellar masses and radii using the scaling relations. We determined the uncertainties on these parameters by propagating the measurement uncertainties of $\nu_{\rm max}$, $\Delta\nu$, and effective temperatures. Our results, alongside the systematic uncertainties, are provided in Table 2. Additionally, we provide uncorrected masses and radii to facilitate studies aimed at calibrating the scaling relation, as these values represent the raw, uncalibrated outputs.

We present the distribution of stellar parameters in Figure 7, which includes data for all stars with a good $\Delta\nu$ flag set to 1 and homogeneous stellar parameters. The distribution spans a range of stellar masses, with a median mass of 1.17 $M_\odot$ (corrected) and 1.23 $M_\odot$ (uncorrected). The uncertainties in mass measurements have a median relative value of 7.2%. The measured radii span the expected range for seismic radii's, with a median relative uncertainty of 2.4%, and align with the trends observed for red giants in earlier catalogues (Yu et al. 2018; Hon et al. 2022). The surface gravities have a median value of 2.45 dex, with a median uncertainty of 0.024 dex, showing the relatively high precision offered by asteroseismic surface gravities. The difference in median mass for stars with spectroscopic parameters from Yu et al. (2023) and Andrae et al. (2023) is 0.01%. This result indicates that stellar masses derived using spectroscopic parameters from the latter are as reliable as those from the former.

4 ANALYSIS

4.1 Properties of catalogue

We present a catalogue of 20,142 oscillating red giants in the TESS CVZ, with consistent and homogeneous measurements. Figure 8 (upper two plots) shows the sky distribution of the stars in our sample. In total, the NCVZ contains 10586 oscillating red giants, while the Southern CVZ contains 9556. The distribution distribution of the

detections on the sky does not show any significant features, apart from a gradient resulting from the higher number of stars towards the Galactic plane.

To ensure reliable measurements, we restrict our analysis in the following sections to 5641 stars with the good $\Delta\nu$ flag set to 1, evolutionary–state scores ≤ 0.1 (clear RGB) or ≥ 0.9 (clear CHeB), and stars where masses and radii were calculated using spectroscopic parameters from Yu et al. (2023), hereafter referred to as the gold sample. Both the full sample and the gold sample span TESS magnitudes from 2 to 13 (Fig. 8 a). In Fig. 8 b, we see a slight excess of stars around $\nu_{\rm max}$ of 9 μHz, possibly due to the Asymptotic Giant Branch stars (AGB) (Dréau et al. 2022). Figure 8 c and d show the precision of $\nu_{\rm max}$ and $\Delta\nu$ for our stars. The median uncertainty in $\nu_{\rm max}$ is 1.2% for the full sample and 1.1% for the gold sample, achieving a precision comparable to *Kepler* data (Yu et al. 2018). For $\Delta\nu$, we achieved a median precision of 1.1% for the full sample, improving to 0.6% for bright stars (Tmag < 8) and 1.3% for stars with Tmag 12. In the gold sample, the median $\Delta\nu$ precision is 0.7%, demonstrating its higher quality relative to the full sample.

4.2 Comparison with GAIA radii and spectroscopic surface gravities

We compared our asteroseismic radii with those derived from the Gaia luminosities by Yu et al. (2023), after correcting for the Gaia parallax zero-point offset. Figure 9 shows the comparison, where the fractional difference between asteroseismic and Gaia radii is plotted for both RGB and CHeB stars. The radii calculated in this work exhibit almost a constant median offset of 0.7% with a scatter of 5.8% up to ≈,15,$R_\odot$ for RGB stars. For CHeB stars, we see an offset of 0.8% with a scatter of 5.5%. Additionally, this scatter is smaller than the typical fractional uncertainty of 7% in Gaia radii, suggesting that the observed scatter is likely dominated by measurement errors in Gaia radii. This result is smaller than the previous reports of an offset of approximately 4% between asteroseismic and Gaia radii (Berger et al. 2018; Zinn 2021; Zinn et al. 2023; Yu et al. 2023).

Figure 9 c compares the surface gravities derived in this work with those obtained from spectroscopy. There is an offset of 0.02 ± 0.08 between asteroseismic and spectroscopic surface gravities, in agreement with previous studies (Thygesen et al. 2012; Morel & Miglio 2012; Yu et al. 2023; Pinsonneault et al. 2025). The results indicate excellent agreement between the two methods.

4.3 Comparison with previous TESS studies

Three previous studies with TESS have carried out asteroseismology of red giants in the Continuous Viewing Zones. Mackereth et al. (2021) conducted a study of red giants in the TESS Southern CVZ from the first year of the mission, which included a region wider than the true CVZ. Using asteroseismic parameters from the Birmingham Asteroseismology Pipeline (BHM) combined with effective temperatures from APOGEE DR17, they derived the masses and radii of approximately 15,000 stars. They then refined the stellar parameters derived from asteroseismic scaling relations using Bayesian optimization with priors from stellar models. Hon et al. (2022) carried out an asteroseismic analysis of 2,600 bright stars in the CVZ that are members of the HD catalogue. Using data from 36 TESS sectors, they measured $\nu_{\rm max}$ and $\Delta\nu$ for 1,700 stars. Their mass and radius estimates were refined using `asfgrid` corrections. Finally, Zhou et al. (2024) used two-minute cadence light curves from TESS to determine $\nu_{\rm max}$ and $\Delta\nu$ for subgiants and red giants. Using stellar atmospheric parameters from Gaia Radial Velocity Spectrometer

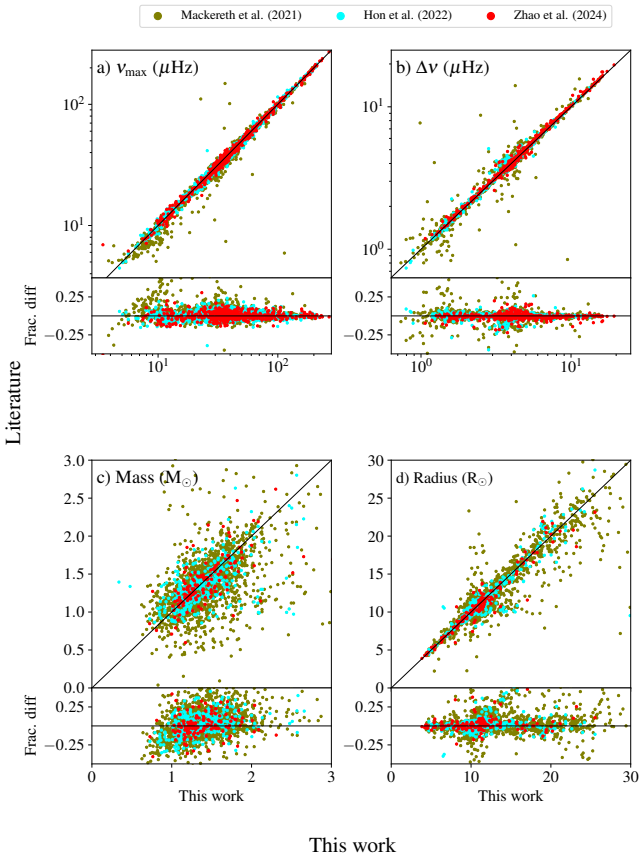

Figure 10. Comparison of asteroseismic and stellar parameters with measurements from previous studies. Red points corresponds to values from Zhou et al. (2024), olive points from Mackereth et al. (2021) and cyan points from Hon et al. (2022). Panel a shows the comparison of $\nu_{\rm max}$ values and panel b shows the comparison of $\Delta\nu$ values. panel c and d represents mass and radius, respectively. The fractional difference is also shown on the bottom axis.

(RVS) spectra, they produced a catalogue of masses and radii for 8,000 solar-like oscillators, some of which are in the CVZs.

We cross-matched our catalogue with these three catalogues of solar-like oscillators to evaluate the level of agreement. Since different studies use varying stellar parameters and correction methods, we used the $\nu_{\rm max}$ and $\Delta\nu$ values from these studies combined with the effective temperatures from our study to derive stellar masses and radii. Figure 10 shows the comparison of asteroseismic and stellar parameters. The $\nu_{\rm max}$ values show excellent agreement, with a discrepancy of less than 1% when compared with Zhou et al. (2024) and Hon et al. (2022), and a median fractional difference of approximately 1.4% when compared with Mackereth et al. (2021). This discrepancy may arise from Mackereth et al. (2021) using a different pipeline to measure $\nu_{\rm max}$. However, the $\Delta\nu$ values from all three studies show consistent agreement, with a variation of less than 0.5%. The derived masses exhibit offsets of 2.2% and 1.5% when compared with Mackereth et al. (2021) and Hon et al. (2022), respectively. These offsets are within the median uncertainty of the mass measurements.

4.4 Comparison with *Kepler* and K2 red giants

The asteroseismic properties of *Kepler* and K2 red giants have been studied extensively, significantly advancing our understanding of

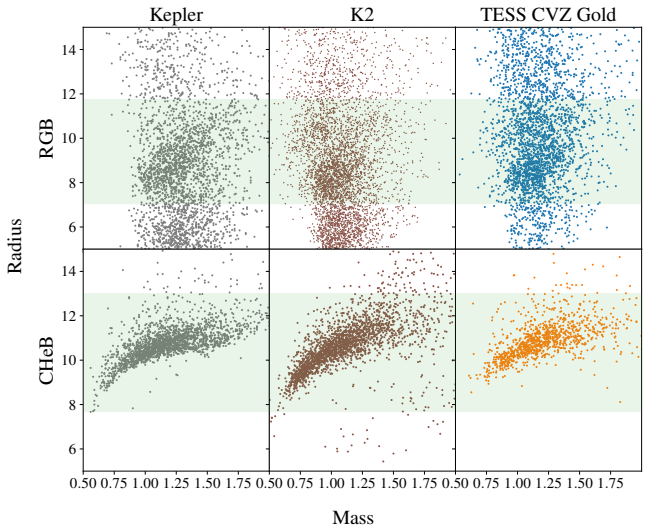

Figure 11. Comparison of the RGB bump and the red clump between *Kepler*, K2 and TESS. The top panel shows the mass–radius plots of the RGB stars and the bottom panel is for CHeB stars. The green shaded region shows the region of RGB bump and CHeB clump.

stellar evolution (Chaplin & Miglio 2013; Hekker & Christensen-Dalsgaard 2017; Jackiewicz 2021; Schonhut-Stasik et al. 2024; Pinsonneault et al. 2025; Noels-Grotsch & Miglio 2025). These properties serve as an important reference point for assessing stellar parameters derived from TESS CVZ observations. Although *Kepler* and K2 targets are located in different regions of the sky, the physical insights gained from their asteroseismic data have been invaluable for understanding red giants. During their ascent along the Red Giant Branch (RGB), stars undergo a brief phase where their luminosity decreases before increasing again. This period of slower luminosity evolution causes an accumulation of stars in a specific region of the observational parameter space, known as the RGB bump. Similarly, when low-mass stars ignite helium in their cores, they form a sharp transition in the Hertzsprung-Russell diagram, referred to as the Zero Age Helium-Burning (ZAHeB) edge (Christensen-Dalsgaard 2015; Hekker & Christensen-Dalsgaard 2017; Girardi 2016). Precise asteroseismic mass–radius (M–R) diagrams from *Kepler* and K2 data have successfully reproduced these sharp features, providing key insights into different stages of stellar evolution and allowing a test of the accuracy of the asteroseismic scaling relations (Li et al. 2021). In this section, we assess whether our TESS CVZ data reveal similar features by comparing them with *Kepler* and K2 datasets (Pinsonneault et al. 2025; Schonhut-Stasik et al. 2024).

The upper panel of Fig. 11 shows the mass–radius diagrams for RGB stars in the *Kepler*, K2, and TESS CVZ samples. In all three samples, the RGB bump occurs in the same region. However, we observe a deficit of low-mass RGB stars in the CVZ sample compared to *Kepler* and K2. Additionally, we identify two subpopulations of RGB stars just above the RGB bump. Since Schonhut-Stasik et al. (2024) used a spectroscopic criterion to determine the evolutionary state of stars, the presence of this feature requires further investigation. The bottom panel of Fig. 11 presents mass-radius diagrams for 1,110 core helium-burning (CHeB) stars in the gold sample. The zero-age CHeB sequence for the CVZ stars is well-aligned with the corresponding *Kepler* CHeB stars. However, comparing the precise location of the ZAHeB edge between *Kepler*, K2, and TESS requires more detailed analysis, which we will address in future work. Interestingly, we also identify a few core helium-burning stars in the CVZ sample that appear to have undergone post-mass-transfer events, consistent with discoveries in *Kepler* data by Li et al. (2022). Determining whether these observed differences arise from genuine population characteristics or observational biases will require future comparisons with synthetic stellar populations.

4.5 Analysis of asteroseismic parameters

The asteroseismic $\log g$ derived in this work allows us to investigate fundamental stellar evolution and validate previous results. Previous studies have demonstrated that asteroseismic $\log g$ provides lower uncertainties compared to spectroscopic $\log g$, making it a more precise measurement (Morel & Miglio 2012; Thygesen et al. 2012; Hekker et al. 2013; Pinsonneault et al. 2014). Such precise constraints help in determining accurate ages as well as calibrating spectroscopic data (Gai et al. 2011; Mészáros et al. 2013; Creevey et al. 2013; Hekker 2018). Figure 12 a shows the Kiel diagram for RGB stars using the asteroseismic $\log g$ and the spectroscopic $\log g$. We observe that the RGB bump is sharper with asteroseismic $\log g$, confirming the accuracy of asteroseismology. As previously observed with CHeB stars, the clump region is evident from asteroseismic $\log g$. However, we identify CHeB stars at $\log g < 2$, a feature not observed in *Kepler* data. We used MIST tracks (Choi et al. 2016) to verify whether CHeB stars can exist at larger radii and found that their positions lie between the Helium flash and Core Helium Burning regions. The typical lifetime ratio of these stars is only 0.002 compared to the CHeB state, suggesting that three stars in our sample may pass through the helium-flashing phase (Bildsten et al. 2011; Deheuvels & Belkacem 2018).

We further explored stellar evolution by plotting various configurations of the Kiel diagram, using $\log g$ as a proxy for the luminosity of stars on the giant branch (Tayar et al. 2019; Pinsonneault et al. 2018, 2025). According to stellar evolution, metallicity affects the locations of the Red Giant Branch (RGB) bump and the CHeB clump (also referred to as the Red Clump, RC) (Kippenhahn et al. 2013; Girardi 2016; Khan et al. 2018; Schonhut-Stasik et al. 2024). Figure 12 c shows the Kiel diagram, with points color-coded by metallicity. At a given $\log g$, we observe that each sequence shifts to higher temperatures as metallicity decreases, indicating that the positions of both the RGB bump and RC vary with stellar metallicity. However, we find that the effect of mass on evolution is not as straightforward as that of metallicity when we color-code the stars based on the asteroseismic mass derived in this work. In the RGB bump and in the CHeB clump, we observe that the location of the bump has a slight dependency on mass. Stars located below the clump have higher masses, confirming that they are secondary clump stars (Girardi 2016).

4.6 Potential for Galactic archaeology

To understand the distribution of stars in our sample within a Galactic context, we analyze their spatial properties in Galactocentric coordinates. Using distances from Gaia DR3 (Gaia Collaboration et al. 2023), we calculate the static Galactocentric positions with the `astropy Galactocentric` module (Blaauw 1960). In this system, the x-axis points from the Sun to the Galactic center in the Galactic plane, the y-axis points toward the direction of Galactic rotation, and the z-axis points toward the Northern Galactic Pole. We adopt a distance of 8.21 kpc from the Sun to the Galactic center and a Cartesian velocity of 233.1 km/s (McMillan 2016). The vertical distance (z)

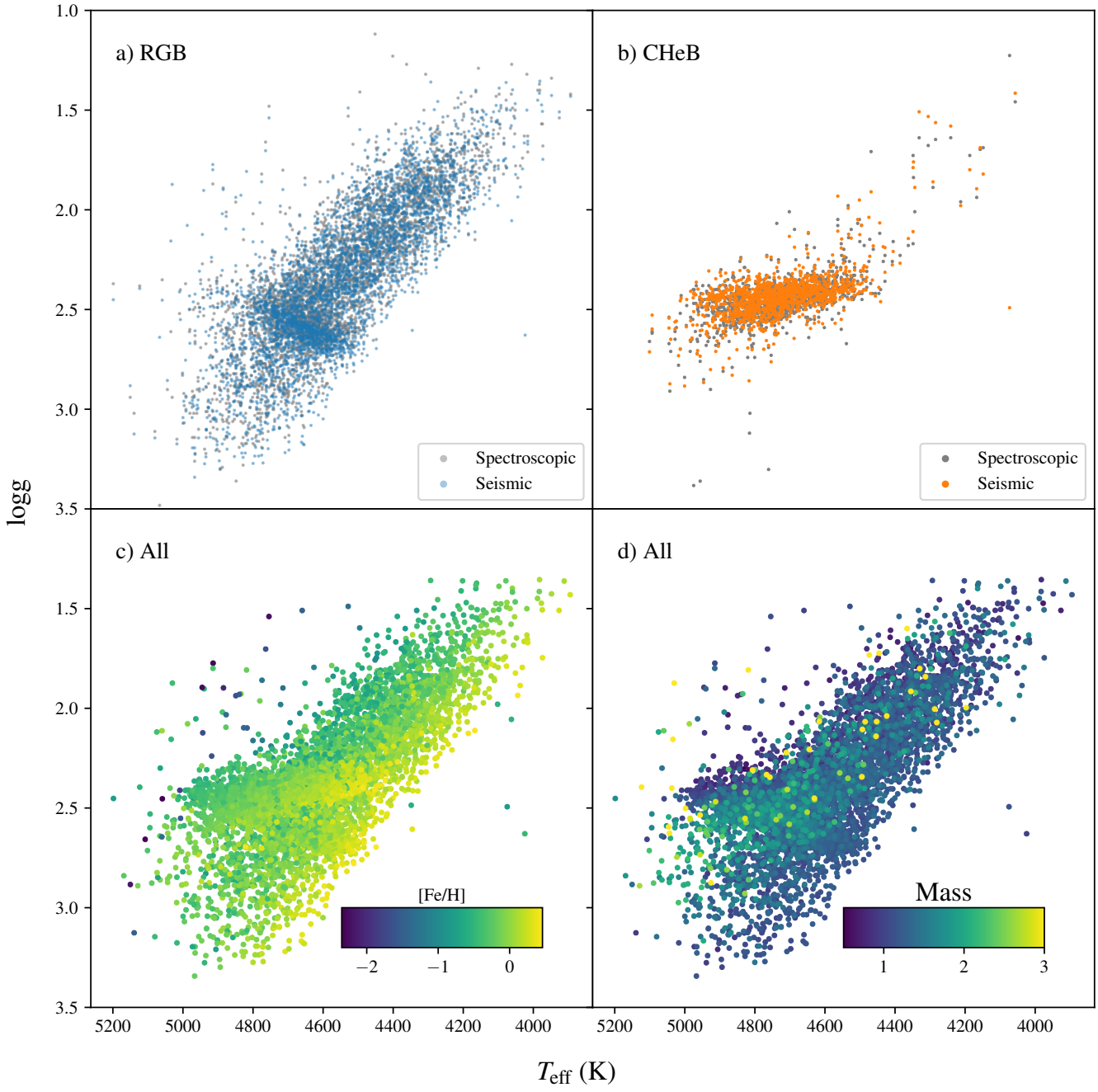

Figure 12. Kiel diagram of the 5641 stars in gold sample. The x-axis represents the effective temperature, while the y-axis corresponds to log g. Panel a illustrates the asteroseismic log g as blue points and the spectroscopic log g as grey points for 4069 RGB stars. Panel b displays the Kiel diagram for 1572 CHeB stars, represented in orange. Panels c and d show the Kiel diagram for all stars, color-coded by metallicity and mass, respectively.

from the Galactic plane depends on stellar age; older stars tend to reside farther from the Galactic plane (Casagrande et al. 2016; Ness et al. 2016). Figure 13 a shows the vertical distance from the Galactic plane as a function of mass. We observe that the average stellar mass increases closer to the plane, confirming that younger stars are generally found closer to the Galactic plane (Chiappini et al. 1997; Miglio et al. 2012; Chiappini 2015; Casagrande et al. 2016; Miglio et al. 2017). Additionally, metal-poor stars are known to reside farther from the Galactic plane, suggesting a metallicity dependence on vertical distance (Carraro et al. 1998; Soubiran et al. 2003, 2008). Figure 13 a demonstrates that metallicity decreases with increasing Z, consistent with previous Galactic studies (Katz et al. 2011; Bovy et al. 2012).

Stars closer to the Galactic plane exhibit higher velocities than those farther from the plane (Haywood et al. 2013). Using proper motions and radial velocities from Gaia DR3 (Gaia Collaboration et al. 2023), we construct the Toomre diagram with Galactocentric velocities (U, V, and W). This diagram is widely used in kinematic studies to analyze the chemistry and dynamics of the Galaxy (Venn et al. 2004). Figure 13 b shows the velocity distribution of red giants

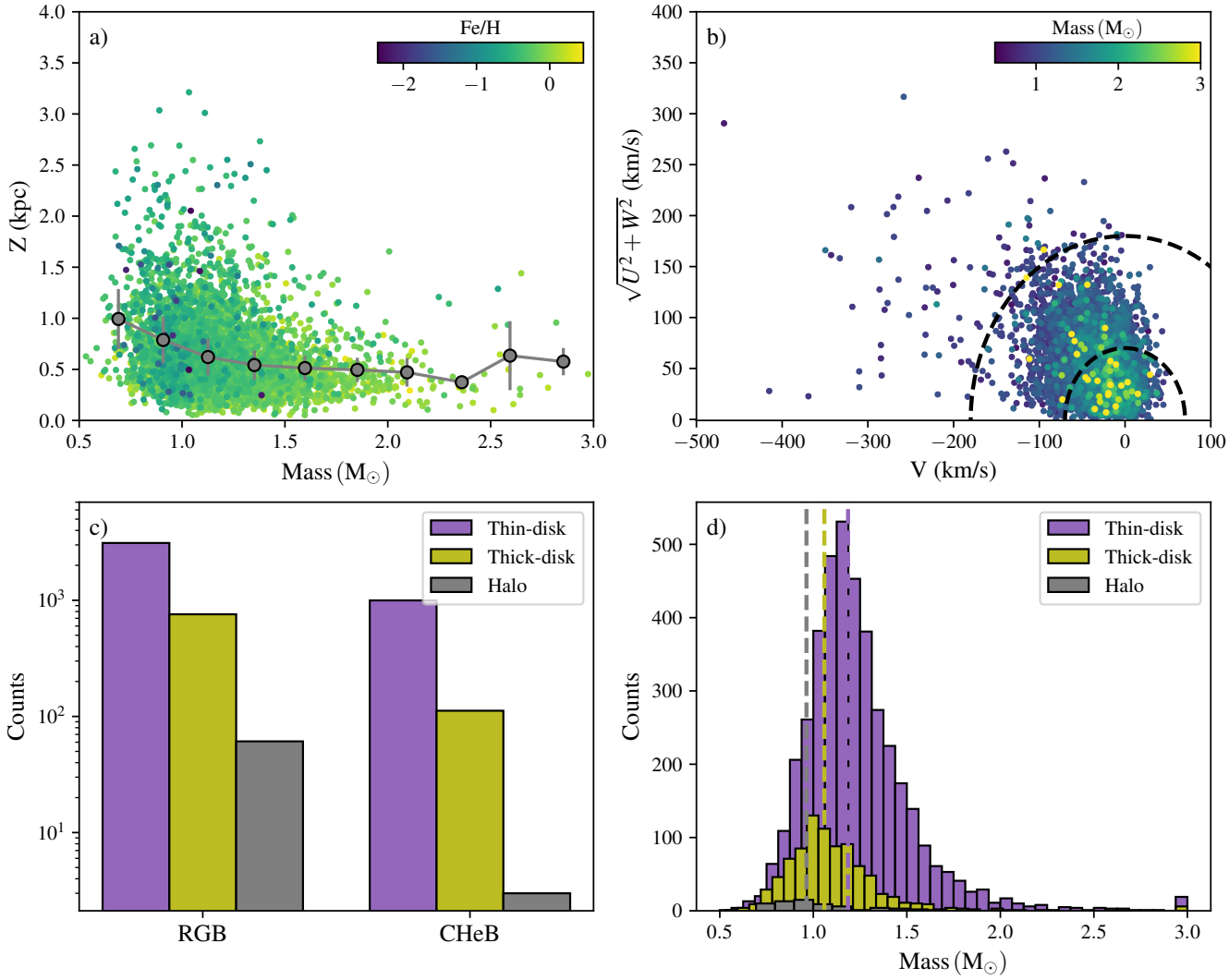

Figure 13. Position of stellar sample in Galactocentric Cartesian coordinates. Panel a shows the positional distribution of all the oscillating stars, colour coded by mass. The solid lines show the median Z per bin and error bars show the median absolute deviation (MAD). Panel b shows the Toomre diagram colour coded by mass. The dashed semi circles show the boundaries from Mardini et al. (2022) used to delineate different populations. Panel c shows the distribution of RGB and CHeB stars in different populations. Panel d shows the distribution of asteroseismic mass in these populations. The vertical dashed lines show the corresponding median mass in each of these populations.

in our sample, where stars are color-coded by asteroseismic mass. We classify the stars into three populations-thin disk, thick disk, and halo-using the total velocities from Mardini et al. (2022). We observe a gradient in stellar mass with the total velocity, arising as a consequence of mass-age-velocity relations (Miglio et al. 2012; Haywood et al. 2013). Based on this classification, our sample contains 4,115 stars in the thin disk, 870 stars in the thick disk, and 64 halo stars. Figure 13 c shows the evolutionary state of the red giants in each population. The total number of stars in each population decreases with distance from the Galactic plane (Read et al. 2024). However, we note a significant reduction in the number of CHeB stars within the halo population. Figure 13 d shows the mass distribution for each stellar population. The median mass decreases from the thin disk to the halo population, which has the lowest velocities. This decrease reflects the age-velocity relation, as lower-velocity stars are typically located farther from the Galactic plane (Chiappini et al. 1997; Haywood et al. 2013). .

5 CONCLUSIONS

In this work, we utilized the long-duration light curves available for the TESS Continuous Viewing Zones to compile a catalogue of 20,142 oscillating red giants. The catalogue provides homogeneously derived frequency of maximum power ($\nu_{\rm max}$), large frequency separation ($\Delta\nu$), evolutionary state classifications, asteroseismic masses, radii, and log g values.

(i) We detected oscillations in 20,142 red giants through manual inspection of TESS light curves. We verified that these stars are oscillating by comparing their properties with theoretical predictions from Chaplin et al. (2011). We observed an increase in the number of stars with high and low $\nu_{\rm max}$ values at fainter magnitudes. This finding suggests two key points: (1) the long-duration light curves from TESS enable the detection of bright red giants at greater distances, facilitating exploration of more distant regions of the sky; and (2)

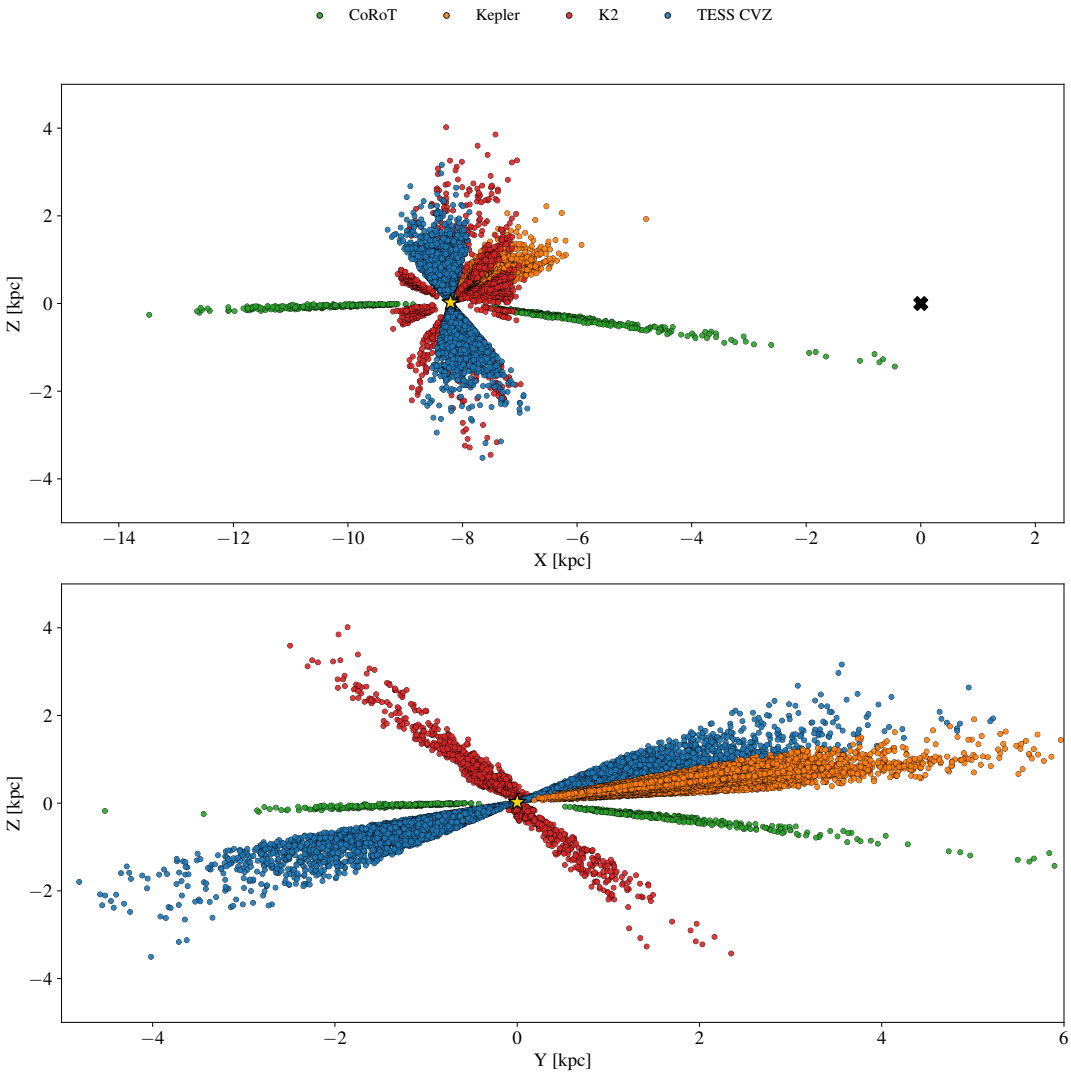

Figure 14. Projection of stars with masses from asteroseismology from various space missions in Galactocentric coordinates. The top panel shows the vertical height from the plane as a function of distance from the galactic centre. The Galactic centre is denoted using a cross symbol. The bottom panel shows the distribution as viewed towards galactic centre. The orange points are *Kepler* data from Pinsonneault et al. (2025), green points for *CoRoT* are from Anders et al. (2017), red points for K2 are from Schonhut-Stasik et al. (2024) and blue points are for TESS CVZ from this work.

extended light curves reduce noise levels, allowing the detection of high $\nu_{\rm max}$ oscillations.

(ii) We obtained $\nu_{\rm max}$ and $\Delta\nu$ for all the stars using `pySYD`, achieving a typical precision of 1.5 % and 1.3 %, respectively. We used the Neural Network framework by Reyes et al. (2022) to assess the reliability of these measurements. For stars with a prediction score from Neural Network above 0.5, we found a typical median uncertainty of 0.9 % in $\Delta\nu$, achieving a precision comparable to that of *Kepler* data.

(iii) We classified the stars into Red Giant Branch (RGB) stars and core Helium-burning (CHeB) stars using the Convolutional Neural Network proposed by Hon et al. (2018b,a). Stars with classification scores below 0.5 were labeled as RGB (denoted by 1), while those with scores above 0.5 were labeled as CHeB (denoted by 2). Contrary to previous studies, we observed CHeB stars with $\nu_{\rm max}$ values as low as 7 μHz. Although this result is unexpected, we do not discard the presence of core Helium-burning stars at such low $\nu_{\rm max}$ values. We labelled these stars as ambiguous, and they warrant further detailed study in the future.

(iv) Using asteroseismic scaling relations, we derived precise masses, radii, and surface gravities for 10987 stars by combining asteroseismic data with spectroscopic parameters from APOGEE, GALAH, RAVE (Yu et al. 2023), and Gaia XP spectra (Andrae et al. 2023). For our analysis, we selected a subsample of 5641 stars, which we labeled the "gold sample". For this sample, we achieved a precision of 7.3 % for mass, 2.8 % for radius, and 0.02 dex for $\log g$.

(v) We find that the masses and radii derived in this study are consistent with the locations of the RGB bump and Zero Age Helium-Burning (ZAHeB) edge observed in previous studies using *Kepler* and K2. As expected, there is a deficit of low-luminosity RGB stars in the Continuous Viewing Zones (CVZ), likely due to observational selection effects. However, simulations according to (Li et al. 2024) are needed to further investigate and confirm the sharpness of the RGB bump and ZAHeB edges. Additionally, we demonstrate that the $\log g$ values derived in this work are more precise than those obtained from spectroscopic measurements, suggesting that they can

serve as a reliable reference for calibrating existing spectroscopic pipelines.

(vi) Combined with Gaia astrometric data, we find that stellar mass decreases with increasing galactic height, consistent with the age-mass relation, where older stars tend to be less massive and dynamically heated to higher altitudes. Furthermore, the average metallicity decreases with increasing distance from the galactic plane. Similar trends are observed in stellar velocities, indicating that the asteroseismic masses derived in this work can serve as a reliable proxy for stellar age.

In summary, this study demonstrates that continuous long-duration photometry from TESS, combined with spectroscopy, enables precise mass estimation, which is crucial for calculating stellar ages (Borre et al. 2022; Morales et al. 2025). A sample with a large number of red giants is valuable for studying the structure and formation of the Milky Way (Chiappini 2015; Hekker 2018; Miglio et al. 2017). Figure 14 shows the projection of stars with asteroseismic ages from different space missions. Previous missions, such as *CoRoT* and K2, focused on regions near the Galactic and ecliptic planes, respectively, while the TESS CVZ data emphasize the ecliptic poles. Combining the data from this work with astrometric data from Gaia allows us to describe the spatial extent of the sample. When integrated with chemical abundances from spectroscopy, this information offers chemo-kinematic insights into the sample (Pinsonneault et al. 2025; Zinn et al. 2022; Roberts et al. 2024; Marasco et al. 2025). Although a detailed analysis lies outside the scope of this paper, we demonstrate that our sample highlights key features relevant to Galactic Archaeology, illustrating its potential scientific value.

ACKNOWLEDGEMENTS

We gratefully acknowledge support from the Australian Research Council through Laureate Fellowship FL220100117. This work has made use of data from the European Space Agency (ESA) mission Gaia (`https://www.cosmos.esa.int/gaia`), processed by the Gaia Data Processing and Analysis Consortium (DPAC, `https://www.cosmos.esa.int/web/gaia/dpac/consortium`). Funding for the DPAC has been provided by national institutions, in particular the institutions participating in the Gaia Multilateral Agreement.

DATA AVAILABILITY

The inclusion of a Data Availability Statement is a requirement for articles published in MNRAS. Data Availability Statements provide a standardized format for readers to understand the availability of data underlying the research results described in the article. The statement may refer to original data generated in the course of the study or to third-party data analysed in the article. The statement should describe and provide means of access, where possible, by linking to the data or providing the required accession numbers for the relevant databases or DOIs.

REFERENCES

Abdurro'uf et al., 2022, ApJS, 259, 35
Anders F., et al., 2017, A&A, 597, A30
Andrae R., Rix H.-W., Chandra V., 2023, The Astrophysical Journal Supplement Series, 267, 8
Baglin A., et al., 2006, in 36th COSPAR Scientific Assembly. p. 3749
Ball W. H., Gizon L., 2014, A&A, 568, A123
Bedding T. R., et al., 2011, Nature, 471, 608
Berger T. A., Huber D., Gaidos E., van Saders J. L., 2018, The Astrophysical Journal, 866, 99
Bildsten L., Paxton B., Moore K., Macias P. J., 2011, The Astrophysical Journal Letters, 744, L6
Blaauw A., 1960, MNRAS, 121, 164
Borre C. C., et al., 2022, MNRAS, 514, 2527
Borucki W. J., et al., 2010, Science, 327, 977
Bovy J., Rix H.-W., Liu C., Hogg D. W., Beers T. C., Lee Y. S., 2012, ApJ, 753, 148
Brown T. M., Gilliland R. L., Noyes R. W., Ramsey L. W., 1991, ApJ, 368, 599
Caldwell D. A., et al., 2020, Research Notes of the American Astronomical Society, 4, 201
Campante T. L., et al., 2016, ApJ, 830, 138
Carraro G., Ng Y. K., Portinari L., 1998, MNRAS, 296, 1045
Carrasco J. M., et al., 2021, A&A, 652, A86
Casagrande L., et al., 2016, MNRAS, 455, 987
Chaplin W. J., Miglio A., 2013, ARA&A, 51, 353
Chaplin W. J., et al., 2011, ApJ, 732, 54
Chen T., Guestrin C., 2016, arXiv e-prints, p. arXiv:1603.02754
Chiappini C., 2015, in EAS Publications Series. EDP, pp 309–341, doi:10.1051/eas/1573006
Chiappini C., Matteucci F., Gratton R., 1997, ApJ, 477, 765
Choi J., Dotter A., Conroy C., Cantiello M., Paxton B., Johnson B. D., 2016, ApJ, 823, 102
Chontos A., Huber D., Sayeed M., Yamsiri P., 2022, The Journal of Open Source Software, 7, 3331
Christensen-Dalsgaard J., 2015, Monthly Notices of the Royal Astronomical Society, 453, 666
Creevey O. L., et al., 2013, Monthly Notices of the Royal Astronomical Society, 431, 2419
De Silva G. M., et al., 2015, Monthly Notices of the Royal Astronomical Society, 449, 2604
Deheuvels S., Belkacem K., 2018, A&A, 620, A43
Dréau G., Lebreton Y., Mosser B., Bossini D., Yu J., 2022, A&A, 668, A115
Elsworth Y., et al., 2019, MNRAS, 489, 4641
Gai N., Basu S., Chaplin W. J., Elsworth Y., 2011, The Astrophysical Journal, 730, 63
Gaia Collaboration et al., 2018, A&A, 616, A1
Gaia Collaboration et al., 2023, A&A, 674, A1
Gal Y., Ghahramani Z., 2016, in Balcan M. F., Weinberger K. Q., eds, Proceedings of Machine Learning Research Vol. 48, Proceedings of The 33rd International Conference on Machine Learning. PMLR, New York, New York, USA, pp 1050–1059, `https://proceedings.mlr.press/v48/gal16.html`
Gehan C., Mosser B., Michel E., Samadi R., Kallinger T., 2018, A&A, 616, A24
Girardi L., 2016, Annual Review of Astronomy and Astrophysics, 54, 95
Grusnis S., Tayar J., Godoy-Rivera D., 2025, The Astrophysical Journal, 993, 96
Guggenberger E., Hekker S., Basu S., Bellinger E., 2016, Monthly Notices of the Royal Astronomical Society, 460, 4277
Hatt E., et al., 2023, A&A, 669, A67
Haywood M., Di Matteo P., Lehnert M. D., Katz D., Gómez A., 2013, A&A, 560, A109
Hekker S., 2018, in Campante T. L., Santos N. C., Monteiro M. J. P. F. G., eds, Astrophysics and Space Science Proceedings Vol. 49, Asteroseismology and Exoplanets: Listening to the Stars and Searching for New Worlds. p. 95 (`arXiv:1711.02178`), doi:10.1007/978-3-319-59315-9_5
Hekker S., Christensen-Dalsgaard J., 2017, A&ARv, 25, 1
Hekker S., et al., 2009, A&A, 506, 465
Hekker S., Elsworth Y., Mosser B., Kallinger T., Basu S., Chaplin W. J., Stello D., 2013, A&A, 556, A59
Hey D., Huber D., Ong J., Stello D., Foreman-Mackey D., 2024, arXiv e-prints, p. arXiv:2403.02489

Hon M., Stello D., Yu J., 2018a, MNRAS, 476, 3233
Hon M., Stello D., Yu J., 2018b, MNRAS, 476, 3233
Hon M., et al., 2021, ApJ, 919, 131
Hon M., Kuszlewicz J. S., Huber D., Stello D., Reyes C., 2022, AJ, 164, 135
Huang C. X., et al., 2020a, Research Notes of the American Astronomical Society, 4, 204
Huang C. X., et al., 2020b, Research Notes of the American Astronomical Society, 4, 206
Huber D., Stello D., Bedding T. R., Chaplin W. J., Arentoft T., Quirion P.-O., Kjeldsen H., 2009, Communications in Asteroseismology, 160, 74
Huber D., et al., 2011, ApJ, 743, 143
Jackiewicz J., 2021, Frontiers in Astronomy and Space Sciences, 7, 102
Jenkins J. M., et al., 2016, in Chiozzi G., Guzman J. C., eds, Society of Photo-Optical Instrumentation Engineers (SPIE) Conference Series Vol. 9913, Software and Cyberinfrastructure for Astronomy IV. p. 99133E, doi:10.1117/12.2233418
Kallinger T., et al., 2010a, A&A, 509, A77
Kallinger T., et al., 2010b, A&A, 522, A1
Katz D., Soubiran C., Cayrel R., Barbuy B., Friel E., Bienaymé O., Perrin M.-N., 2011, A&A, 525, A90
Khan S., Hall O. J., Miglio A., Davies G. R., Mosser B., Girardi L., Montalbán J., 2018, ApJ, 859, 156
Kippenhahn R., Weigert A., Weiss A., 2013, Stellar Structure and Evolution, doi:10.1007/978-3-642-30304-3.
Kjeldsen H., Bedding T. R., 1995, A&A, 293, 87
Kjeldsen H., Bedding T. R., Christensen-Dalsgaard J., 2008, ApJ, 683, L175
Larsen J. R., et al., 2025, A&A, 697, A153
Li Y., Bedding T. R., Stello D., Sharma S., Huber D., Murphy S. J., 2021, MNRAS, 501, 3162
Li Y., et al., 2022, Nature Astronomy, 6, 673
Li Y., et al., 2023, MNRAS, 523, 916
Li Y., et al., 2024, ApJ, 974, 77
Liagre B., et al., 2025, A&A, 702, A144
Lundkvist M. S., et al., 2025, arXiv e-prints, p. arXiv:2510.11532
Mackereth J. T., et al., 2021, MNRAS, 502, 1947
Marasco C., Tayar J., Nidever D., 2025, The Astrophysical Journal, 986, 144
Mardini M. K., Frebel A., Chiti A., Meiron Y., Brauer K. V., Ou X., 2022, The Astrophysical Journal, 936, 78
McMillan P. J., 2016, Monthly Notices of the Royal Astronomical Society, 465, 76
Miglio A., et al., 2012, Monthly Notices of the Royal Astronomical Society, 429, 423
Miglio A., et al., 2017, Astronomische Nachrichten, 338, 644
Morales L. M., Tayar J., Claytor Z. R., 2025, ApJ, 986, 229
Morel T., Miglio A., 2012, Monthly Notices of the Royal Astronomical Society: Letters, 419, L34
Mosser B., et al., 2013, A&A, 550, A126
Mosser B., Vrard M., Belkacem K., Deheuvels S., Goupil M. J., 2015, A&A, 584, A50
Mosser B., Pinçon C., Belkacem K., Takata M., Vrard M., 2017, A&A, 600, A1
Mészáros S., et al., 2013, The Astronomical Journal, 146, 133
Ness M., Hogg D. W., Rix H.-W., Martig M., Pinsonneault M. H., Ho A. Y. Q., 2016, The Astrophysical Journal, 823, 114
Noels-Grotsch A., Miglio A., 2025, The Golden Gift of Red Giants. 2514-3433, IOP Publishing, doi:10.1088/2514-3433/adcf15, https://doi.org/10.1088/2514-3433/adcf15
Paegert M., Stassun K. G., Collins K. A., Pepper J., Torres G., Jenkins J., Twicken J. D., Latham D. W., 2022, VizieR Online Data Catalog: TESS Input Catalog version 8.2 (TIC v8.2) (Paegert+, 2021), VizieR On-line Data Catalog: IV/39. Originally published in: 2021arXiv210804778P
Paparrizos J., Gravano L., 2017, ACM Trans. Database Syst., 42
Pinsonneault M. H., et al., 2014, ApJS, 215, 19
Pinsonneault M. H., et al., 2018, ApJS, 239, 32
Pinsonneault M. H., et al., 2025, ApJS, 276, 69
Press W. H., Rybicki G. B., 1989, ApJ, 338, 277
Read A. K., et al., 2024, Monthly Notices of the Royal Astronomical Society, 528, 2464
Reyes C., Stello D., Hon M., Zinn J. C., 2022, Monthly Notices of the Royal Astronomical Society, 511, 5578
Ricker G. R., et al., 2015, Journal of Astronomical Telescopes, Instruments, and Systems, 1, 014003
Roberts J. D., et al., 2024, MNRAS, 530, 149
Schonhut-Stasik J., et al., 2024, AJ, 167, 50
Sharma S., Stello D., Bland-Hawthorn J., Huber D., Bedding T. R., 2016, ApJ, 822, 15
Soubiran C., Bienaymé O., Siebert A., 2003, A&A, 398, 141
Soubiran C., Bienaymé O., Mishenina T. V., Kovtyukh V. V., 2008, A&A, 480, 91
Sreenivas K. R., Bedding T. R., Li Y., Huber D., Crawford C. L., Stello D., Yu J., 2024, MNRAS, 530, 3477
Sreenivas K. R., Bedding T. R., Huber D., Crawford C. L., Stello D., Pedersen M. G., Li Y., Hey D., 2025, MNRAS, 537, 3265
Steinmetz M., et al., 2020, AJ, 160, 83
Stello D., Sharma S., 2022, Research Notes of the American Astronomical Society, 6, 168
Stello D., Bruntt H., Preston H., Buzasi D., 2008, ApJ, 674, L53
Stello D., Chaplin W. J., Basu S., Elsworth Y., Bedding T. R., 2009, MNRAS, 400, L80
Stello D., et al., 2013, ApJ, 765, L41
Stello D., et al., 2017, The Astrophysical Journal, 835, 83
Stello D., et al., 2022, MNRAS, 512, 1677
Tayar J., Beck P. G., Pinsonneault M. H., García R. A., Mathur S., 2019, ApJ, 887, 203
Thygesen A. O., et al., 2012, A&A, 543, A160
Ulrich R. K., 1986, ApJ, 306, L37
Venn K. A., Irwin M., Shetrone M. D., Tout C. A., Hill V., Tolstoy E., 2004, AJ, 128, 1177
Vrard M., Mosser B., Samadi R., 2016, A&A, 588, A87
White T. R., Bedding T. R., Stello D., Christensen-Dalsgaard J., Huber D., Kjeldsen H., 2011, The Astrophysical Journal, 743, 161
Yu J., Huber D., Bedding T. R., Stello D., Hon M., Murphy S. J., Khanna S., 2018, ApJS, 236, 42
Yu J., Khanna S., Themessl N., Hekker S., Dréau G., Gizon L., Bi S., 2023, ApJS, 264, 41
Zhou J., et al., 2024, ApJS, 271, 17
Zinn J. C., 2021, AJ, 161, 214
Zinn J. C., et al., 2022, ApJ, 926, 191
Zinn J. C., Pinsonneault M. H., Bildsten L., Stello D., 2023, MNRAS, 525, 5540

This paper has been typeset from a TEX/LATEX file prepared by the author.